RSC Advances

PAPER

View Article Online
View Journal | View Issue

Cite this: *RSC Adv.*, 2025, **15**, 25233

Research on the mechanism of mechanochemical activation for enhanced leaching of vanadium-bearing shale: activation kinetics and fluorine adsorption

Xuxia Zhao,[abcd] Yimin Zhang,*[abcd] Nannan Xue*[abcd] and Pengcheng Hu[abcd]

Vanadium-bearing shale as a strategic resource is an important raw material for extracting vanadium, and the mechanochemical activation can realize the vanadium extraction by full-wet leaching with green, low-carbon and high efficiency. Based on mineralogical research on mineral composition and distribution, mineral embedded grain size distribution, we employ a graded activation process. The mechanism of mechanochemical activation-enhanced dissolution of vanadium-bearing shale is revealed through the relationship between activation kinetics and vanadium leaching as well as the fluorine adsorption process on different minerals surfaces of vanadium-bearing shale. Vanadium-bearing shale is mainly composed of quartz, muscovite, calcite, pyrite, feldspar and apatite. Vanadium with 94.24% exists in muscovite, while the remaining 5.76% exists in oxide. Muscovite is predominantly closely associated with quartz, calcite and organic carbonaceous and tends to be enriched in fine grained, displaying fine disseminated granularity with 0.005–0.06 mm. The grindability order of vanadium-bearing shale is observed as follows: −3 to +2.5 mm < −2.5 to +2 mm < −2 to +1 mm < −1 to +0.6 mm. The activation process of different particle sizes were well evaluated by kinetic equations (R^2 = 0.99). The vanadium leaching efficiency has a positive linear relationship with the activation yield at the optimal leaching particle size with −0.6 mm. The vanadium leaching efficiency and activation time can be expressed by equation of $\eta = \gamma_0 \exp(-kt^n)\mu + \nu$. The mineral surface of vanadium-bearing shale has a good adsorption of F^- (23.89 mg g^{-1}) undergoing amorphous phenomena. The order of F^- adsorption capacity is calcite, pyrite, dolomite, muscovite, feldspar, and quartz. The adsorption process of F^- alters the surface potential on the vanadium-bearing shale, and the negative charge on the of muscovite surface increases, while that of pyrite and calcite decreases, which is conducive to the diffusion of H^+ to the surface of muscovite and away from pyrite and calcite. F^- generates CaF_2 with the surface of calcite and FeF_3 with Fe(III)–S on the surface of pyrite, hindering and slowing down the dissolution of calcite and pyrite. F^- forms Al–F and Si–F bonds with Si and Al on the surface of muscovite, promoting the dissolution of muscovite.

Received 5th June 2025
Accepted 10th July 2025

DOI: 10.1039/d5ra03987h

rsc.li/rsc-advances

1. Introduction

Vanadium is included in the strategic metal lists of China, America, and the European Union and is widely used in the aerospace, metallurgy, chemical, medicine, and new energy industries.[1] Vanadium-bearing shale is a polymetallic ore with vanadium grades ranging from 0.1 to 1.2%.[2,3] The gross reserves of V_2O_5 in vanadium-bearing shale are approximately 118 million tons, accounting for more than 87% of the domestic reserves of vanadium,[4,5] which is the crucial raw material for the extraction of vanadium. Primary vanadium-bearing shale is a sedimentary rock rich in organic carbon, argillaceous materials, and sulfides, mainly composed of quartz, mica, calcite and pyrite. Vanadium in vanadium-bearing shale mainly exists in silicate minerals in the form of low-valent isomorphism and is difficult to be released.

Except thermal activation, mechanochemical activation is another pretreatment method of enhancing mineral leaching.[6–8] The mechanochemical activation refers to the changes in the physical and chemical properties and crystal structure of solids under the action of external forces such as

[a]School of Resource and Environmental Engineering, Wuhan University of Science and Technology, Wuhan 430081, Hubei Province, China. E-mail: zym126135@126.com; cbdis@aliyun.com
[b]State Environmental Protection Key Laboratory of Mineral Metallurgical Resources Utilization and Pollution Control, Wuhan 430081, Hubei Province, China
[c]Collaborative Innovation Center of Strategic Vanadium Resources Utilization, Wuhan 430081, Hubei Province, China
[d]Hubei Provincial Engineering Technology Research Center of High Efficient Cleaning Utilization for Shale Vanadium Resource, Wuhan 430081, Hubei Province, China

shearing, friction, impact and extrusion.[9] Through plastic deformation and defect formation, part of the mechanical energy is converted into the internal energy of the solid, putting it in a high-energy unstable state and causing an increase in the chemical reactivity of the solid, thus inducing physicochemical reactions process.[10] Mechanical force disordered the solid crystal structure, resulting in dislocation formation and flow of atoms within solid particles, thereby causing the amorphous transformation of the particles.[11,12] During the amorphous process, the internal energy stored in solid particles is much greater than that stored in simple dislocations, and they are in a high-energy unstable state.[13] Therefore, this is also the reason for the enhanced reactivity and accelerated reaction rate of solid particles.[14] Unlike ordinary thermochemical reactions, mechanochemical reactions is mechanical energy rather than thermal energy, the reactions can be completed without harsh conditions such as high temperature and high pressure.[15] Its advantages of good reaction safety and low energy consumption are also major advantages of mechanochemical technology over high-temperature heat treatment.[16,17]

Mechanical activation is the process of reducing ore particle size under the action of mechanical force.[18] Under the action of mechanical force, mechanical energy is directly transferred from the ball mill to the solid system, causing the minerals to be crushed and the particle size of large solid particles to decrease.[19] Due to differences in mineral characteristics, during the process of activation, the parameters of ore particle size, grindability, and crushing energy are particularly important to the activation performance of ore.[18,20] Therefore, it is necessary to study the activation kinetics and particle size characteristics of these materials.[21,22] One study compared the crushing processes of quartz and chlorite by grinding kinetics during wet ball milling.[23] At the same time, the time required to crush the particles to obtain the appropriate particle size is a necessary step in designing the activation process.[24,25] In our previous studies,[26] the mechanochemical activation pretreated the vanadium-bearing shale to effectively improve the leaching efficiency of vanadium and achieves a full hydro-metallurgical process. It was discovered that the activation time is an important factor of affecting the leaching and the particle size and monomer dissociation of vanadium-bearing shale is closely related to activation time. Meanwhile, during the ball milling process, an activator is added, the reactivity of activation is enhanced through the collision, friction and shearing of the spheres, promoting the interaction between the activator and the minerals. Inorganic reagents are utilized to adsorb the mineral solids, thereby altering the physical and chemical properties of the mineral surface.[27]

In this study, we investigated the process mineralogy of vanadium-bearing shale, examining mineral composition, dissemination relationships, and vanadium occurrence. Furthermore, we analyzed the impacts of graded activation processes on vanadium leaching. We established activation kinetics and a vanadium leaching efficiency model for activation efficiency for vanadium-bearing shale, laying a theoretical foundation for enhancing vanadium leaching efficiency and optimizing activation conditions and performance. Meanwhile, the fluorine adsorption on surfaces of vanadium-bearing shale was revealed using pure minerals under mechanical chemical activation process.

2. Experimental

2.1 Materials

The vanadium-bearing shale examined in this study originated from a mine in Hubei Province, Central China, and underwent pulverization to achieve a grain size of 0–3 mm prior to analysis. Chemical compositions of the raw ore, detailed in Table 1, reveal a V_2O_5 grade of 0.72%, with silicon, aluminum, calcium, and iron as the primary non-target elements. Specifically, SiO_2, Al_2O_3, CaO, Fe_2O_3, MgO, and K_2O contents were 60.69%, 8.99%, 11.14%, 3.52%, 1.71%, and 1.88%, respectively, indicating a multi-calcium vanadium-bearing shale. Identified mineral phases in the vanadium-bearing shale include mica, quartz, calcite, and apatite (Fig. 1), with calcite predominating as the gangue mineral with high acid consumption. Furthermore, Fig. 2 demonstrates a significant correlation between vanadium and silicon, aluminum, potassium, and magnesium, suggesting muscovite as the primary host for vanadium. Therefore, the vanadium-bearing shale utilized in this study serves as a representative example of mica-type vanadium-bearing shale.

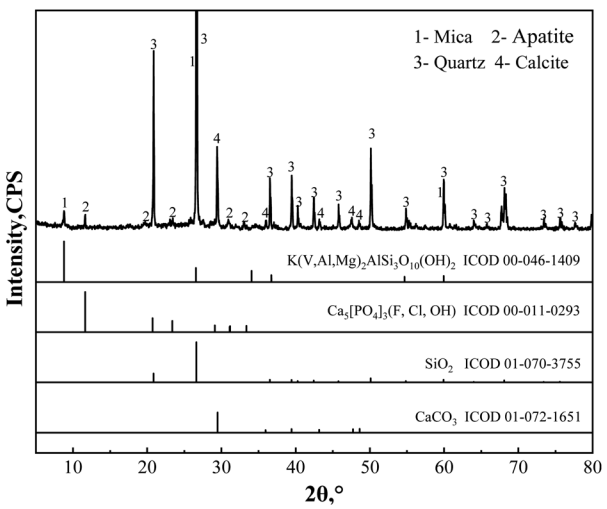

Fig. 1 XRD patterns of the raw vanadium-bearing shale.

Table 1 Chemical compositions of the vanadium-bearing shale

Composition	V_2O_5	SiO_2	Al_2O_3	CaO	Fe_2O_3	MgO	K_2O	S	BaO	P	ZnO	Na_2O	TiO
Content/%	0.72	60.69	8.99	11.14	3.52	1.71	1.88	1.39	0.58	0.52	0.29	0.22	0.21

2.2 Experiments

Particle size screening experiments were conducted using a top strike type vibrating screen machine (HLSDOB-Φ200, Wuhan Hengle Mineral Engineering Equipment Co., Ltd, China). In each trial, 100 g of vanadium-bearing shale was introduced into the vibrating screen and subjected to screening for a duration of 5 min.

Under the specified activation conditions—such as a pulp concentration of 50%, a ball-to-pulp ratio of 50, and a 5 wt% NaF activator—vanadium-bearing shale samples with different particle sizes (500) underwent testing at varying activation durations. This was achieved through conical ball milling (HLXMQ-Φ150 × 50, Wuhan Hengle Mineral Engineering Equipment Co., Ltd, China) and rod milling (HLXMB-Φ200 × 240). Following activation, the product was filtered, dried, and subjected to particle size analysis using both a vibrating screen and a laser particle size analyzer.

The leaching efficiency of vanadium was obtained through an acid leaching experiment. The vanadium-bearing shale (50 g) and 30 wt% sulfuric acid were put into a 250 mL conical bottle, oscillated and leached for 12 h in a thermostatic oscillator with a vibration velocity of 200 rpm and a temperature of 95 °C (SHA-2, Jiangsu Jintan Yitong Electronics Co., Ltd). After the leaching was completed, the leaching residue and vanadium-containing leachate were obtained by solid–liquid separation, and the vanadium concentration in the leachate was determined by ammonium ferric sulfate titration.

2.3 Characterization

The chemical composition of the vanadium-bearing shale was detected by an inductively coupled plasma optical emission spectrometer (ICP, Horiba Ultima Expert: Agilent ICP-OES 730, US). The mineral phase compositions of the vanadium-bearing shale were tested by X-ray diffraction (XRD, D/MAX-RB, Rigaku, Japan). The micromorphology and elemental distribution of the vanadium-bearing shale were analyzed by scanning electron microscopy (SEM, JSM-IT300, JEOL, Tokyo, Japan) on an instrument equipped with an X-square energy dispersive spectrometer (EDS, OXFORD, Britain). The mineral dissemination relationship of vanadium-bearing shale was tested by a polarizing microscope (Nikon, LV100POL). The particle size of the activated vanadium-bearing shale was tested by a laser particle sizer (ZEN2600, Malvern Instruments Ltd). The dissemination patterns of the V element in the vanadium-bearing shale obtained by the Advanced Mineral Identification and Characterization System (MLA, Sigma 300, Quantax 400 and AMICS).

3. Results and discussion

3.1 Characteristics analysis of vanadium-bearing shale

3.1.1 Dissemination relationship of vanadium-bearing shale. The optical microscopy images of the vanadium-bearing shale are shown in Fig. 3. Quartz and calcite are associated with carbonaceous and clay minerals in granular and veined forms, and the particle sizes are 0.005–0.20 mm (Fig. 4(a)

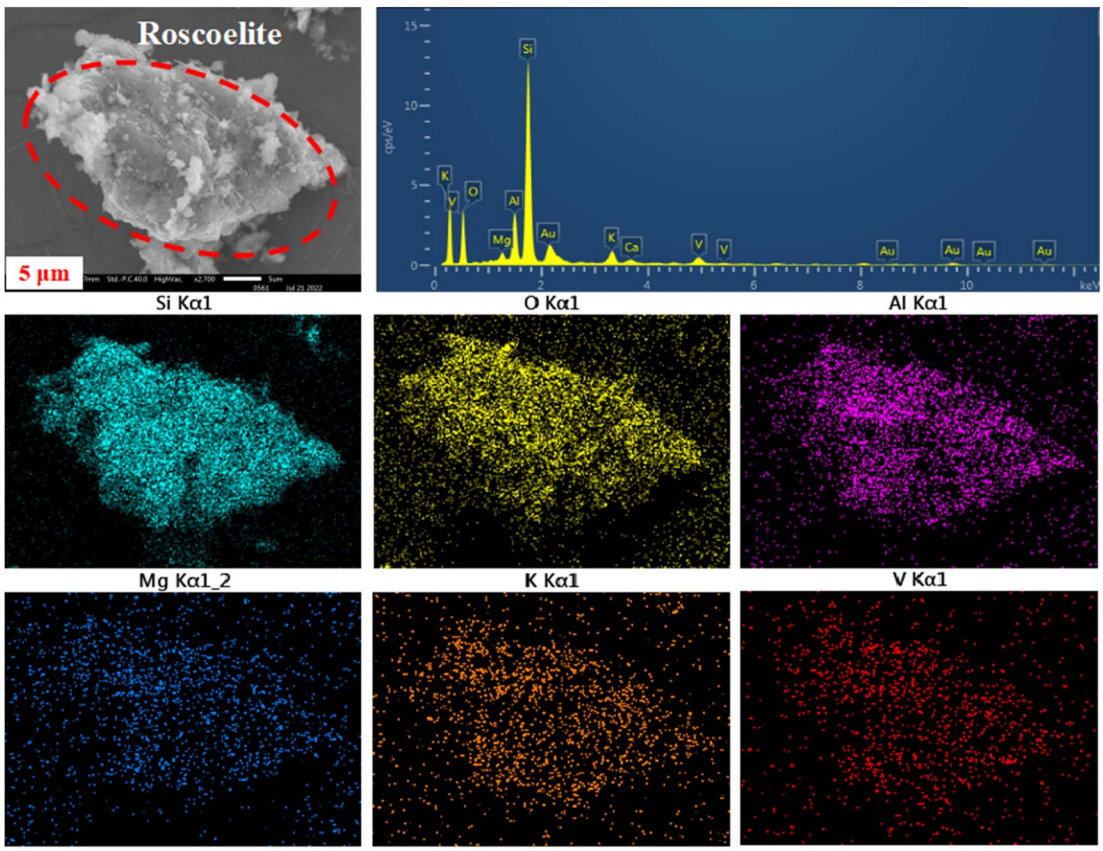

Fig. 2 Microstructure and elemental mapping images of the vanadium-bearing shale.

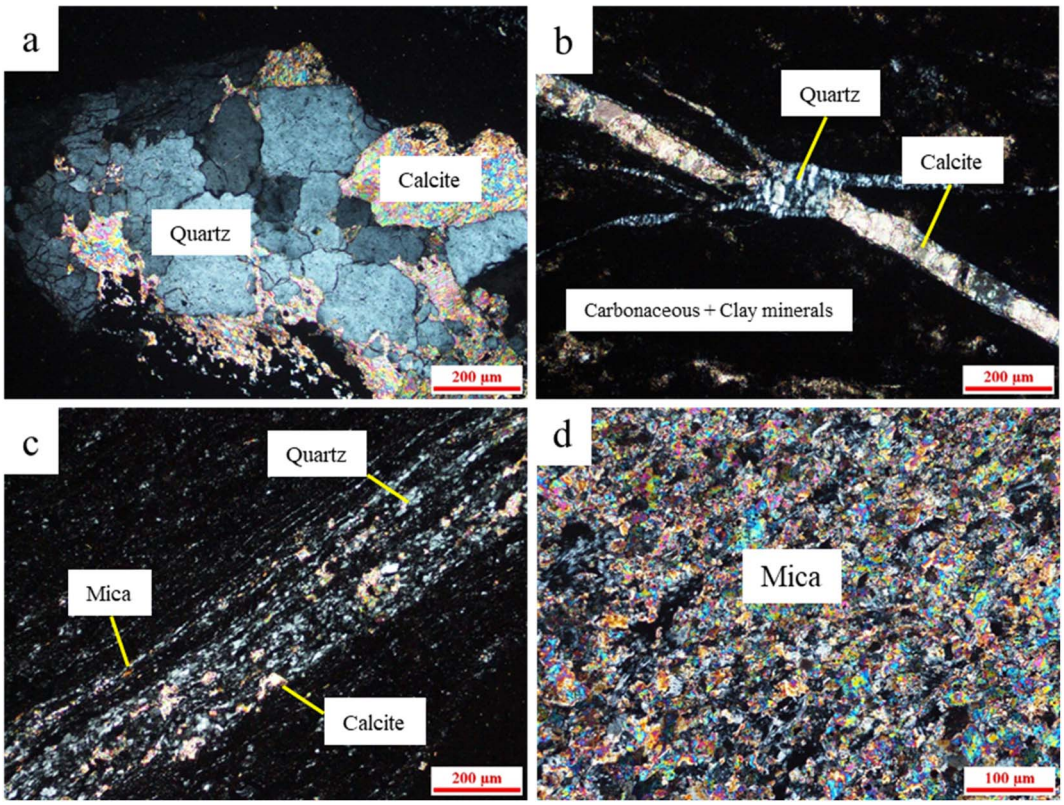

Fig. 3 Optical microscopy images of vanadium-bearing shale. (a) Granular quartz and calcite. (b) Calcite and quartz were distributed in fine veins. (c) Mica, quartz, and calcite distributed in bands. (d) Sericite aggregate.

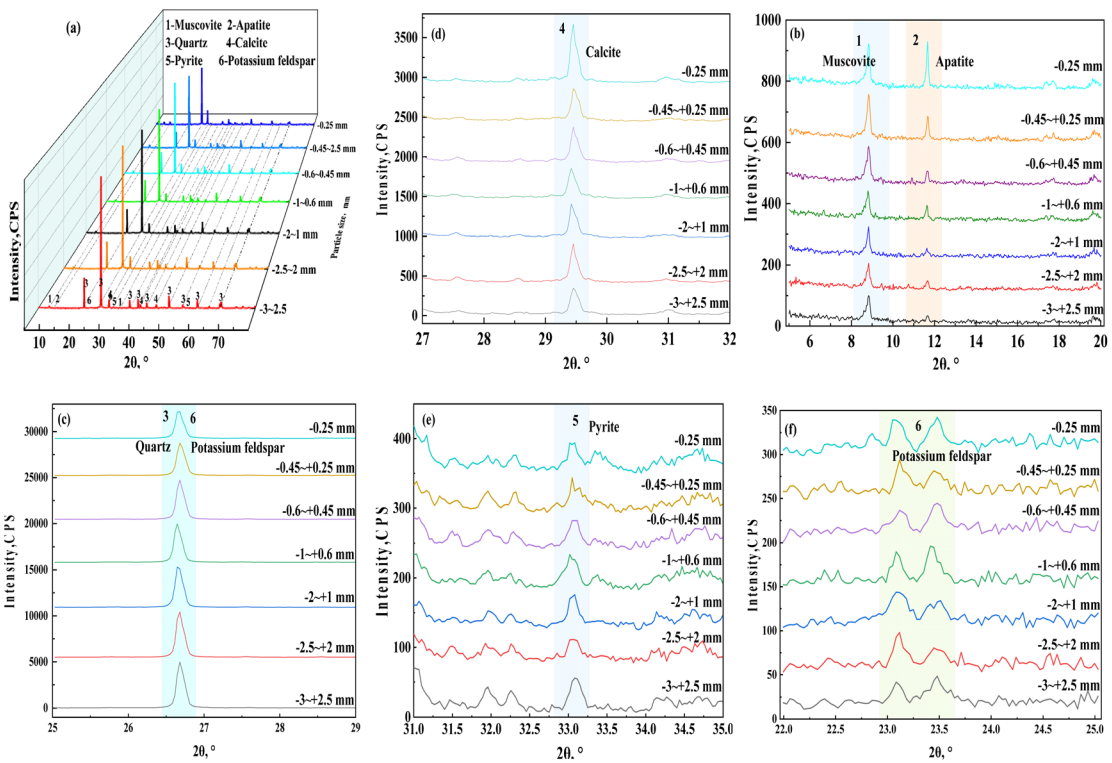

Fig. 4 XRD patterns of the vanadium-bearing shale with different particle size ((a): full spectrum; (b): muscovite and apatite; (c): quartz and potash feldspar; (d): calcite; (e): pyrite; (f): potassium feldspar).

Table 2 Occurrence relationship of vanadium in vanadium-bearing shale

Element	Muscovite	V-oxide	Total
V	94.24	5.76	100

and (b)). The muscovite is a fine scaly aggregate, which has a more scattered directional distribution in quartz schistosity and foliation, and the slice diameter is 0.005–0.06 mm (Fig. 4(c) and (d)). In addition, organic carbonaceous is mainly concentrated in fine aggregates and linearly distributed along the interstices of plates or in densely distributed or cemented quartz fragments, ranging in size from 0.001 mm to 0.60 mm, which affects the transfer process of the medium during acid leaching due to its hydrophobicity. As shown in Table 2, only 5.76% of vanadium occurs in oxides, while 94.24% of vanadium occurs in muscovite as isomorphism in vanadium-bearing shale, it is due to the high octahedral selective energy of V^{3+}, which replaces Al^{3+} in mica octahedra by isomorphism.

3.1.2 Minerals distribution of vanadium-bearing shale. The vanadium-bearing shale is a very complex ore, the mineral composition is shown in Table 3. The main minerals are quartz, mica, calcite, pyrite, potassium feldspar and apatite, the content of which are 62.04%, 12.95%, 6.50%, 3.07% and 2.63%, respectively, accounting for more than 87% of the total vanadium-bearing shale. The organic carbon content is 8 wt%, which indicated that the ores a kind of high-carbon primary vanadium-bearing shale.

The particle size distribution of the raw vanadium-bearing shale was examined, and the distribution of vanadium across different particle sizes was investigated. Standard screens with mesh sizes of 2.5 mm, 2 mm, 1 mm, 0.6 mm, 0.45 mm, and 0.25 mm were utilized to categorize the raw vanadium-bearing shale into seven size ranges, including particle sizes of −3 to +2.5 mm, −2.5 to +2 mm, −2 to +1 mm, −1 to +0.6 mm, −0.6 to +0.45 mm, −0.45 to +0.25 mm, and −0.25 mm, respectively. The particle size and vanadium distribution of the vanadium-bearing shale are presented in Table 4, the yields of vanadium-bearing shale with different particle sizes are different. The V_2O_5 grade is different for the various vanadium-bearing shale particle sizes, and the vanadium grade increases with decreasing particle size.

The phase analysis of vanadium-bearing shales with different particle sizes were conducted on, as shown in Fig. 4. In Fig. 4(a), the main phases of each granulometric class of vanadium shale is composed of muscovite, quartz, apatite, calcite, pyrite and potassium feldspar. The XRD characteristic peaks of muscovite, apatite and calcite increase with the decrease of particle size in Fig. 4(b) and (d), indicating that muscovite, apatite and calcite are gradually enriched in the fine-grained grade. Specially, muscovite is consistent with the distribution of vanadium grade. On the contrary, the characteristic peaks of quartz weakens as the particle size decreases in Fig. 4(c), indicating quartz is enriched in the coarse-grained grade. According to the characteristic peaks of pyrite and potassium feldspar in Fig. 4(e) and (f), pyrite and potassium feldspar are distributed relatively evenly in each grain size. The minerals distribution of vanadium-bearing shale with different particle sizes are shown in Table 5. With the particle size of vanadium-bearing shale decreasing, the content of quartz reduce from 72.28 to 50.92 wt%, while muscovite, calcite, apatite and carbonaceous increase from 11.42 to 14.36 wt%, 4.04 to 9.07 wt%, 0.52 to 3.25 wt% and 5.05 to 11.41 wt%, respectively.

The distribution characteristics of various minerals in vanadium-bearing shale are related to disseminated grain size and hardness of the minerals. The Mohs hardness of main minerals are shown in Table 6. The order of mineral hardness

Table 3 Mineral composition and contents in the vanadium-bearing shale (wt%)

Mineral	Quartz	Muscovite	Calcite	Pyrite	Potassium feldspar	Apatite
Content	62.04	12.95	6.5	3.07	2.63	1.98
Mineral	Dolomite	Akermanite	Magnetite	Barite	Anhydrite	Gedrite
Content	0.72	0.7	0.33	0.34	0.22	0.23
Mineral	V-oxide	Szomolnokite	Hematite	Rutile	Organic carbon	—
Content	0.19	0.03	0.05	0.03	8	—

Table 4 Particle size distribution of vanadium-bearing shale and vanadium grade

Particle size (mm)	Yield (%)	V_2O_5 grade (%)	Distribution rate of V_2O_5 (%)	Mohs hardness
−3 to +2.5	12.16	0.44	7.50	6
−2.5 to +2	9.64	0.52	7.01	6
−2 to +1	25.83	0.59	22.91	6
−1 to +0.6	16.07	0.73	16.22	6
−0.6 to +0.45	6.52	0.81	7.31	5.5
−0.45 to +0.25	9.71	0.89	12.00	
−0.25	20.07	1.03	28.76	
Total	100.00	0.72	100.00	

Table 5 Minerals distribution of vanadium-bearing shale with different particle sizes (wt%)

	Particle size (mm)				
Minerals	−3 to +2.5	−2.5 to +2	−2 to +1	−1 to +0.6	−0.6
Quartz	72.28	70.88	67.79	64.89	50.92
Muscovite	11.42	11.78	12.27	12.72	14.36
Calcite	4.04	4.19	5.11	6.15	9.07
Pyrite	2.51	2.43	2.46	2.28	4.21
Potassium feldspar	2.35	2.44	2.43	2.36	3.04
Apatite	0.52	0.83	1.36	1.91	3.25
Dolomite	0.24	0.97	0.48	1.06	0.84
Barite	0.78	0.34	0.32	0.12	0.32
Gedrite	0.19	0.21	0.23	0.25	0.23
Akermanite	0.28	0.3	0.41	0.57	1.22
Anhydrite	0.11	0.21	0.23	0.23	0.24
Vanadium oxide	0.2	0.16	0.1	0.18	0.34
Magnetite	0.03	0.07	0.11	1.05	0.33
Hematite	0	0	0	0	0.14
Szomolnokite	0	0	0	0	0.08
Carbonaceous + clay	5.05	5.19	6.7	6.23	11.41
Total	100.00	100.00	100.00	100.00	100.00

Table 6 Mohs hardness of minerals[28]

Minerals	Quartz	Pyrite	Potassium feldspar	Apatite	Calcite	Muscovite
Mohs hardness	7	6–6.5	6	5	3	2–3

from high to low is as follows: quartz, pyrite, potassium feldspar, calcite and muscovite. During the coarse crushing process of vanadium-bearing shale, due to the different hardness of minerals, the particle size changes to varying degrees. The particle size change of quartz with high hardness is relatively small, while the particle size of minerals with lower hardness, such as mica and calcite, are finer. Meanwhile, the finer the embedding particle size, the more enriched towards the fine-grained. Additionally, the larger the dissemination particle size, the more enriched towards the coarse-grained. Hence, the quartz in vanadium-bearing shale is not only hard but also has a large dissemination particle size, so it is enriched in the coarse-grained grade. While the muscovite, calcite and apatite vanadium-bearing shale are enriched in the fine-grained grade.

3.1.3 Optimal leaching particle size of vanadium-bearing shale. To clarify the connection between particle size distribution and leaching, we examined the vanadium leaching efficiency of various particle sizes of vanadium-bearing shale, the results are depicted in Fig. 5. Within the −3 to +0.25 mm range, there is an inverse relationship between vanadium leaching efficiency and particle size, as shown in Fig. 5(a). Conversely, as particle size decreases, vanadium leaching efficiency increases. However, when the particle size drops to −0.25 mm, vanadium leaching efficiency decreases. This indicates that excessively

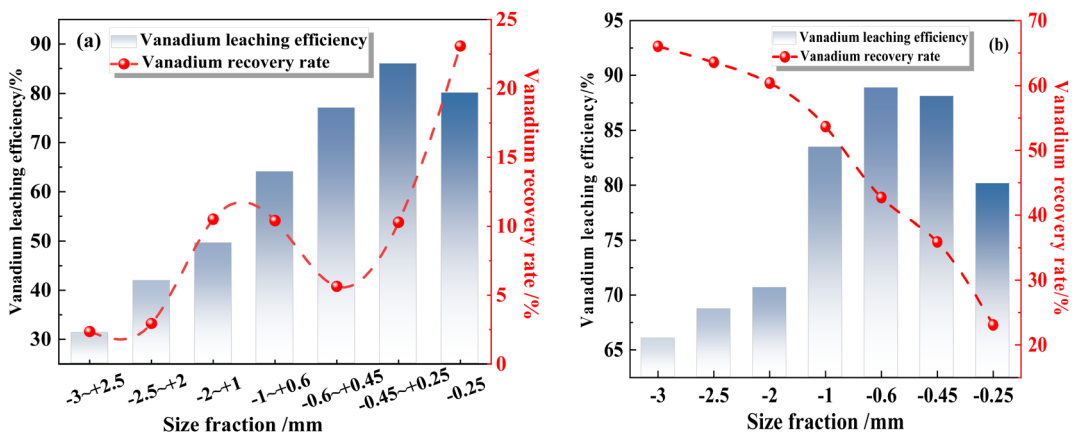

Fig. 5 The vanadium leaching efficiency for different particle sizes with 30 wt% H_2SO_4, 5 wt% CaF_2, a leaching temperature of 98 °C and a leaching time of 12 h ((a) narrow particle size and (b) wide particle size).

fine particle size of vanadium-bearing shale hampers vanadium leaching. Hence, it is crucial to isolate the vanadium mica mineral monomer and control the particle size of vanadium shale through activation. In Fig. 5(b), both coarse and fine particles exhibit low vanadium leaching efficiency, whereas intermediate particles demonstrate higher efficiency. Direct acid leaching yields a vanadium leaching efficiency of over 88% when the particle size is −0.6 mm. Coarse-grained vanadium-bearing mica, enclosed by quartz and other minerals, remains undissolved during leaching, hindering vanadium release. In fine-grained vanadium-bearing shale, calcite, an acid-consuming mineral, competes with mica for dissolution, depleting hydrogen ions and resulting in low vanadium leaching efficiency. Moreover, finer particles tend to agglomerate, impeding leaching. Hence, the optimal leaching particle size is −0.6 mm. Vanadium-bearing shale is segregated into two size fractions: −0.6 mm particles undergo direct leaching, while +0.6 mm particles undergo activation to enhance vanadium recovery. Gradual activation reduces vanadium-bearing shale processing capacity by 36%, thereby cutting energy consumption during activation.

As shown in Fig. 6, according to the correlation between vanadium leaching efficiency and mineral distribution in vanadium-bearing shale, the vanadium leaching efficiency shows a good positive correlation with the content distribution of muscovite ($R^2 = 0.98$). In addition, the distribution of quartz, muscovite and calcite is relatively good correlation ($R^2 = 0.99$). Among which quartz is negatively correlated, while muscovite and calcite are positively correlated.

3.2 Effect of mechanochemical activation on particle size distribution

3.2.1 Full-particle size activation. To explore the effect of the activation method under activation time on the particle size distribution of vanadium-bearing shale, activation time experiments were carried out under a feed particle size of −3 mm, with the activation time varying from 1 to 10 min. The yields of vanadium-bearing shale under different activation times are shown in Fig. 7.

Fig. 7(a) indicated that with the increase in activation time, the yield of coarse fraction with particle size of −3 to +0.6 mm decreased rapidly and the yield of fine fraction with −0.6 mm increased gradually. Fig. 7(b) illustrated that the negative cumulative yield of finer fraction increased rapidly with the gradual increase in activation time. The cumulative curves of particle size distribution showed that the curve was convex, and the breakage products were mainly coarse particles. In addition, the proportion of fine-grained powder is high, the particle size distribution is wide, and the coarse particle content is reduced from 12.16% to 4.74% and not wholly broken. There were two possibilities for this phenomenon, one is that the crushing rate of fine particle size is larger than that of coarse ones, and the other is that the crushing process of vanadium-bearing shale belongs to surface crushing.

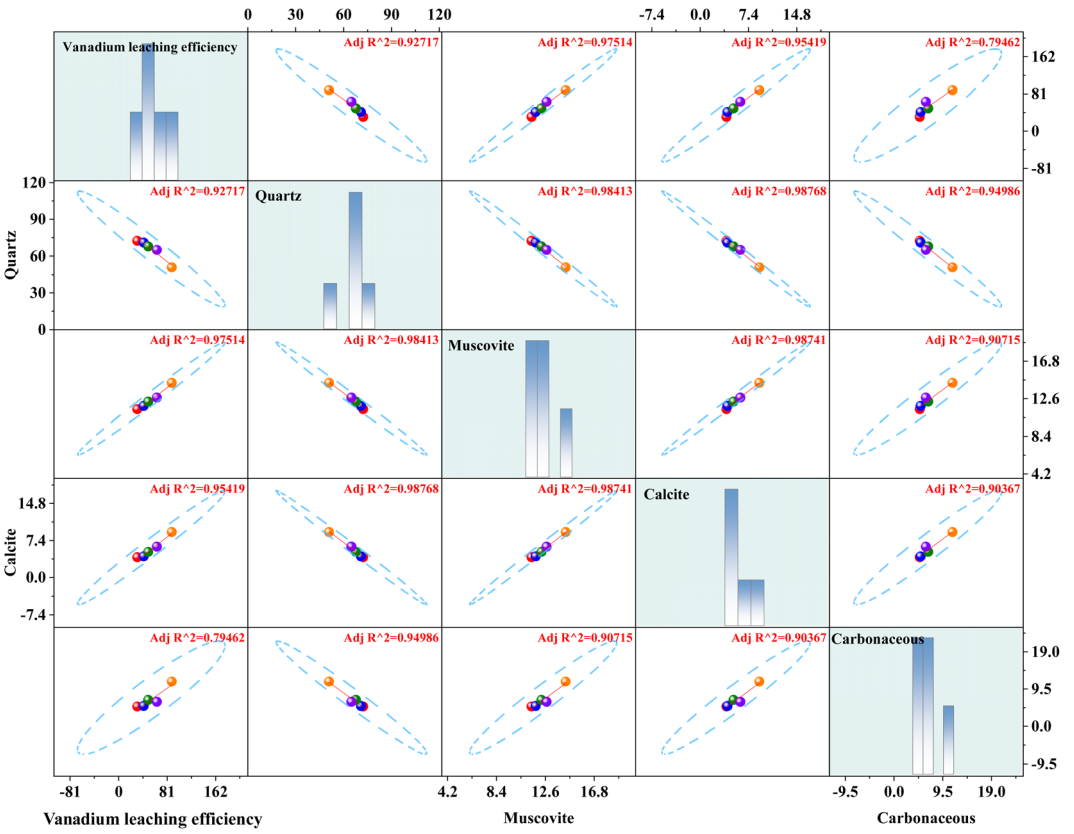

Fig. 6 The correlation between vanadium leaching and mineral distribution.

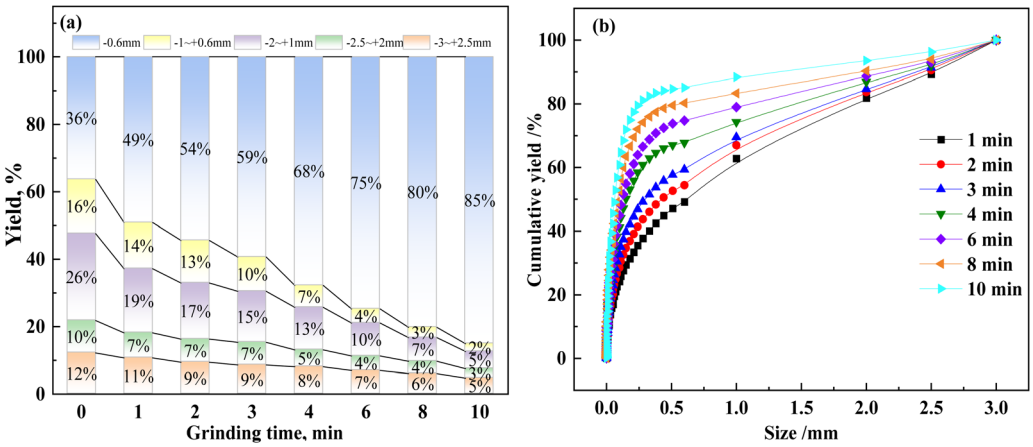

Fig. 7 Effect of activation time on the yields of vanadium-bearing shale ((a): yield; (b): cumulative yield).

3.2.2 Graded activation. To elucidate the activation characteristics of vanadium-bearing shale with various particle sizes, we investigated graded activation of the shale. Vanadium-bearing shale with a particle size of 0–3 mm was sieved into grain sizes of −3 to +2.5 mm, −2.5 to +2 mm, −2 to +1 mm, −1 to +0.6 mm, and −0.6 mm. Activation time experiments were conducted on vanadium-bearing shale with grain sizes of −3 to +2.5 mm, −2.5 to +2 mm, −2 to +1 mm, and −1 to +0.6 mm. The activation yields and accumulation curve under different activation times are depicted in Fig. 8.

As seen in Fig. 8(a)–(d), there is a swift decline in the content of coarse particle sizes (−3 to +2.5 mm, −2.5 to +2 mm, −2 to +1 mm, and −1 to +0.6 mm) with activation time, while the proportion of −0.6 mm particles increases during activation. The yields of vanadium-bearing shale vary notably across different particle sizes, with smaller particles demonstrating superior activation efficiency. In addition, intermediate particle-grade products are generated during the activation process, as shown in Fig. 8(a)–(c). With increasing activation time, these intermediate particles are gradually crushed into fine particles, which indicates that the whole particle is destroyed by volume destruction; thus, producing intermediate particles. Moreover, the variation in the yield of intermediate-sized particles has no obvious trend of increasing or decreasing with increasing activation time, which shows that the activation process is relatively uniform for each particle size of vanadium-bearing shale.

As depicted in Fig. 8(e)–(h), the negative cumulative yield of vanadium-bearing shale with various particle sizes increased with activation time, though the curve variations exhibited slight differences. The negative cumulative yield curve of vanadium-bearing shale with a particle size of −3 to +2.5 mm displayed an S-shaped pattern, indicating that during activation, particles were mainly distributed in the fine size range of −0.6 mm and the coarse size range of −3 to +2.5 mm, with the intermediate size range showing minimal but uniform distribution (Fig. 8(e)). With prolonged activation time, the curves of the other three particle sizes gradually transitioned from convex to concave, suggesting a gradual enrichment of coarse particles into finer ones (Fig. 8(f)–(h)).

3.2.3 Activation kinetics of vanadium-bearing shale. The activation kinetic model is based on the activation speed. In the activation process, the value of remaining material on the screen passing through a certain particle size is directly proportional to the initial material value. Activation efficiency and activation time can be expressed as follows:[29,30]

$$\gamma = \gamma_0 \exp(-kt^n) \quad (1)$$

where, γ_0 is the initial activation materials with certain particle size and n is the time index determined by the nature of material and its activation conditions. k is the activation rate constant.

The linear equation can be obtained by mathematical transformation of eqn (1):

$$\ln\left(\ln\left(\frac{\gamma_0}{\gamma}\right)\right) = \ln k + n \ln t \quad (2)$$

The functional relationship between kinetic parameters n, k and particle size d can be expressed as follows:

$$k(d) = A_0 + A_1 d^{x_1} \quad (3)$$

$$n(d) = C_0 + C_1 d^{x_2} \quad (4)$$

where, A_0, A_1, C_0, C_1, x_1 and x_2 are the coefficients to be determined, respectively, depending on the nature of the material to be ground and the activation conditions. The parameter n mainly depends on the homogeneity of the material and the particle size characteristics.

Activation kinetics experiments of vanadium-bearing shale were conducted to characterize the effect of different particle sizes on ore breakage. Based on the kinetic equations, the kinetic parameters n and k were obtained by fitting. Fig. 9(a) shows the grinding kinetics results for particle sizes of −3 to +0.6 mm, and Fig. 9(b)–(e) show the grinding kinetics for feed sizes of −3 to +2.5 mm, −2.5 to +2 mm, −2 to +1 mm and −1 to

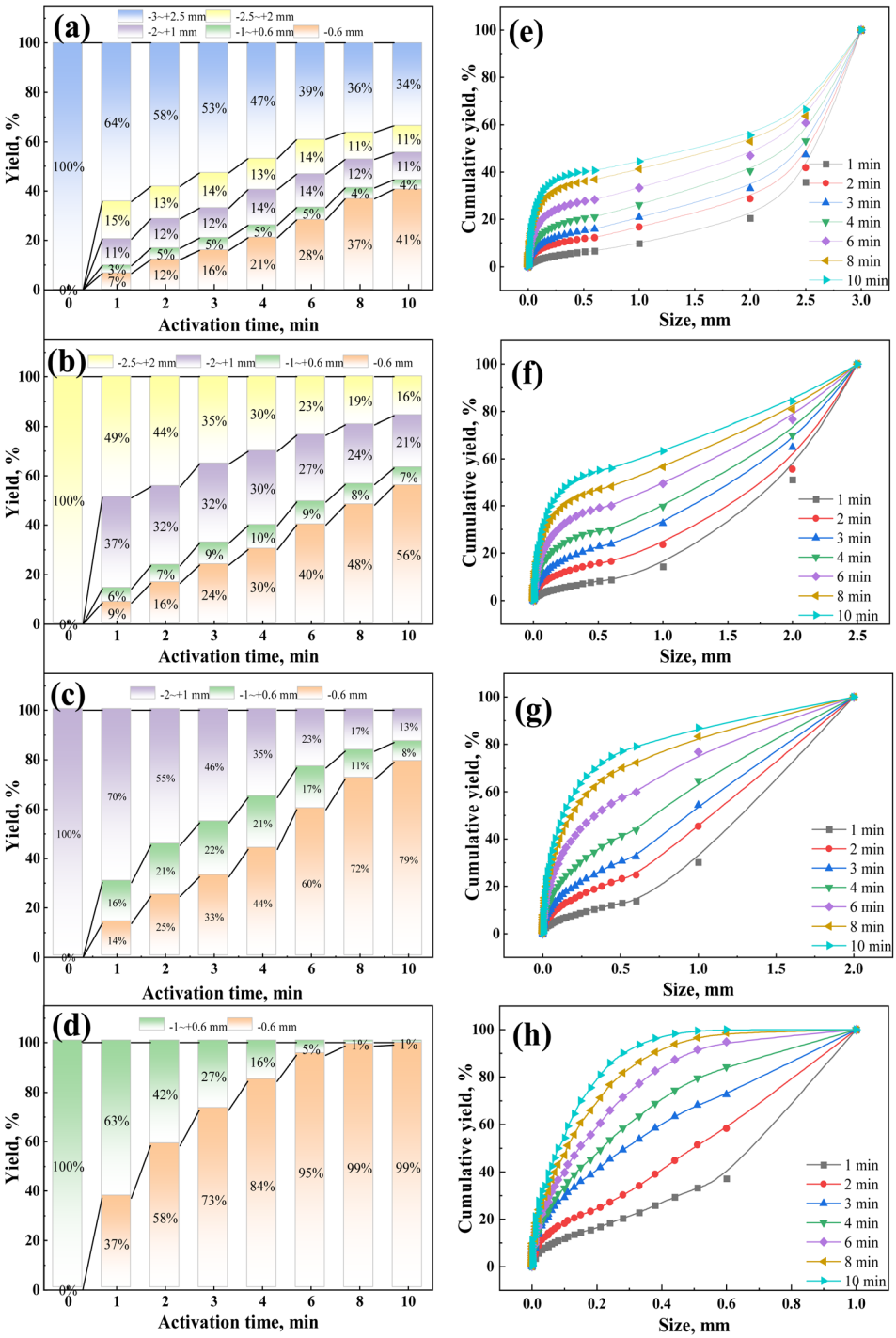

Fig. 8 The yields and cumulative yields of different particle size distribution under different activation times (graded particle size: (a and e): −3 to +2.5 mm; (b and f): −2.5 to +2 mm; (c and g): −2 to +1 mm; (d and h): −1 to +0.6 mm).

+0.6 mm, respectively. The grinding kinetic parameters n and k are shown in Table 3. Fig. 10(a)–(d) showed the curves of the relationships between the activation kinetics parameters n and k and the particle size d.

Fig. 10 illustrates the quantitative description of vanadium-bearing shale through activation kinetic equations, achieving a fitting accuracy of 0.99. The parameters n and k are determined by the material's characteristics and activation conditions. The n value primarily reflects the material's homogeneity and strength, indicating its grindability. A higher n suggests that the ore can be activated easily,[31] and a lower n implies greater difficulty in activation. The activation fineness determines the k value. When activation time (t) is less than $e^{1/k}$, k predominantly influences the cumulative yield on sieve (γ). A higher k corresponds to a smaller γ, resulting in a greater reduction of γ and faster activation efficiency.[29]

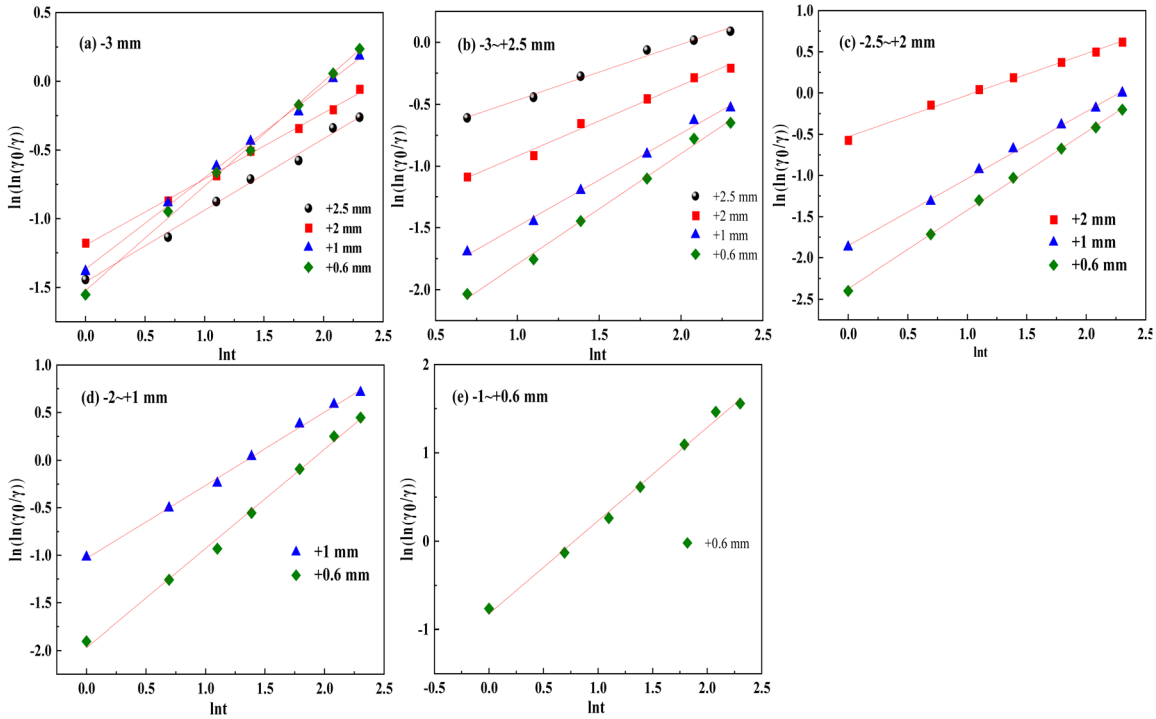

Fig. 9 Fitting curve of the grinding kinetics of vanadium-bearing shale (feed particle size: (a): −3 to +0.6 mm; (b): −3 to +2.5 mm; (c): −2.5 to +2 mm; (d): −2 to +1 mm; (e): −1 to +0.6 mm).

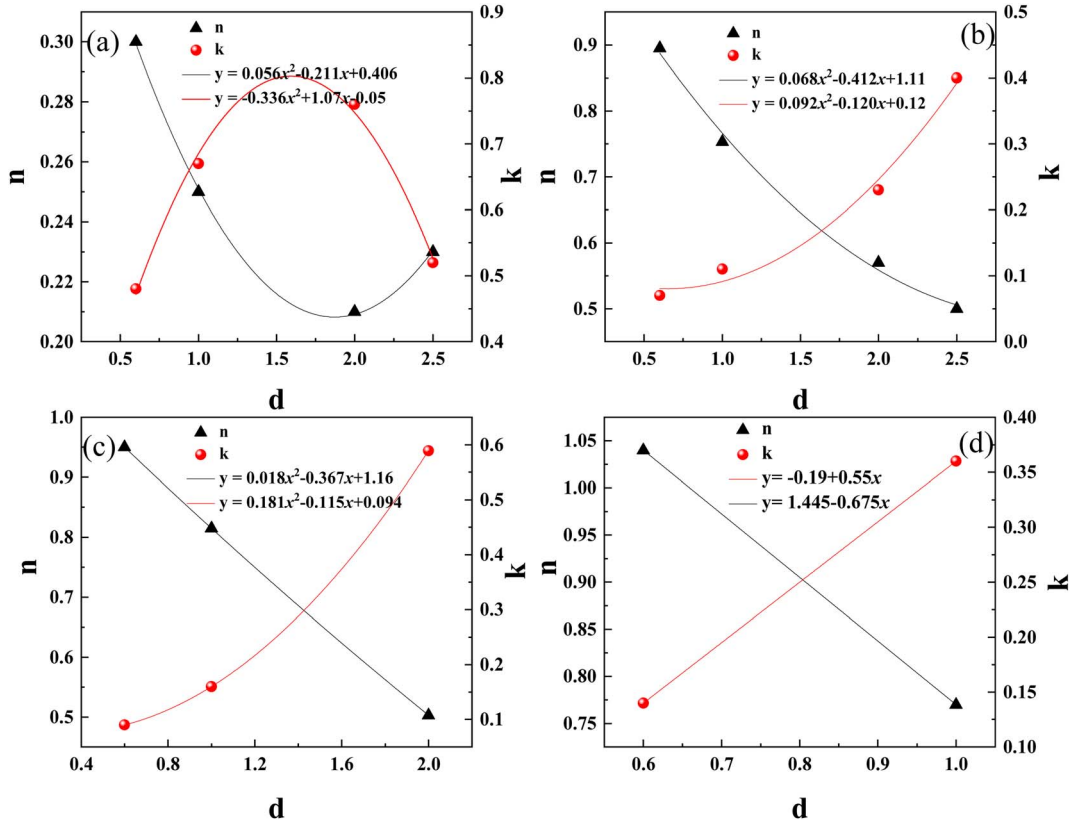

Fig. 10 The curve of the relationship between the grinding kinetics parameters *n* and *k* and the particle size *d* (feed particle size: (a): −3 mm; (b): −3 to +2.5 mm; (c): −2.5 to +2 mm; (d): −2 to +1 mm).

Table 7 Fitting parameters of the kinetic model of vanadium-bearing shale with different feed particle sizes

Kinetic equation		n order kinetic model		
Feed size (mm)	Particle size (mm)	n	k	R^2
−3	−3 to +2.5	0.52	0.23	0.994
	−2.5 to +2	0.76	0.21	0.998
	−2 to +1	0.67	0.25	0.998
	−1 to +0.6	0.48	0.30	0.997
−3 to +2.5	−3 to +2.5	0.50	0.40	0.987
	−2.5 to +2	0.57	0.23	0.988
	−2 to +1	0.75	0.11	0.995
	−1 to +0.6	0.90	0.07	0.994
−2.5 to +2	−2.5 to +2	0.50	0.59	0.995
	−2 to +1	0.82	0.16	0.998
	−1 to +0.6	0.95	0.09	0.999
−2 to +1	−2 to +1	0.77	0.36	0.997
	−1 to +0.6	1.04	0.14	0.995
−1 to +0.6	−1 to +0.6	1.06	0.44	0.994

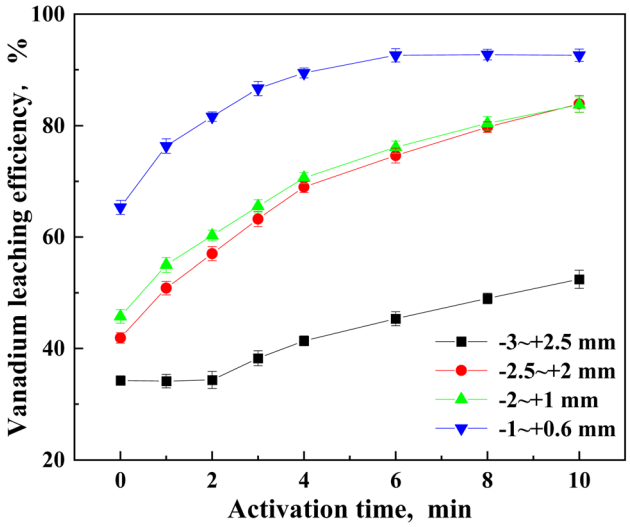

Fig. 11 Effect of activation time of graded vanadium-bearing shale on vanadium leaching efficiency.

As depicted in Table 7, vanadium-bearing shale exhibits improved grindability with finer particle sizes, making it easier to grind. During the activation process, the material often forms a multiparticle layer between the activation media. The force exerted by the media on the material can be transmitted through these particles, potentially without direct contact, leading to breakage. During mixed crushing, the particle size of the fragile material is smaller than that during single crushing, and the particle size during difficult crushing is larger than that during single crushing. With graded activation, the crushing yield of coarse particles is greater than that with mixed activation. Thus, graded activation is exceedingly necessary to improve the activation efficiency and prevent the overactivation of fine particles.

The activation kinetic parameters n and k for different particle sizes were obtained by fitting the data in Table 3. Thus, the optimal activation kinetic equation of vanadium-bearing shale of different sizes is obtained, as shown in eqn (5)–(9).

$$-3\ \text{mm}: \gamma = \gamma_0 \exp[(0.336d^2 - 1.07d + 0.05)\, t^{(0.056d^2-0.211d+0.406)}] \quad (5)$$

$$-3\ \text{to}\ +2.5\ \text{mm}: \gamma = \gamma_0 \exp[(-0.029d^2 + 0.12d - 0.12)\, t^{(0.068d^2-0.412d+1.11)}] \quad (6)$$

$$-2.5\ \text{to}\ +2\ \text{mm}: \gamma = \gamma_0 \exp[(-0.181d^2 + 0.115d - 0.094)\, t^{(0.018d^2-0.367d+1.16)}] \quad (7)$$

$$-2\ \text{to}\ +1\ \text{mm}: \gamma = \gamma_0 \exp[(-0.19 + 0.55d)t^{(1.44-0.68d)}] \quad (8)$$

$$-1\ \text{to}\ +0.6\ \text{mm}: \gamma = \gamma_0 \exp(0.44t^{1.06}) \quad (9)$$

3.3 The relationship between activation yield and vanadium leaching efficiency

3.3.1 Effect of graded activation on vanadium leaching efficiency. The vanadium leaching efficiency of vanadium-bearing shale with different particle sizes at different activation times was investigated. Leaching tests were conducted on vanadium-bearing shale with coarse-grained sizes of −3 to +2.5 mm, −2.5 to +2 mm, −2 to +1 mm and −1 to +0.6 mm under different activation time. The leaching conditions were as follows: 15 vol% H_2SO_4, liquid–solid ratio 1.5 L kg^{-1}, leaching temperature 95 °C and leaching time 12 h. The leaching results of graded activation of vanadium-bearing shale are shown in Fig. 11. The vanadium leaching efficiency of vanadium-bearing shale with different particle sizes increased with the increase of activation time. Except that the leaching curves of the two particle sizes of −2.5 to +2 and −2 to +1 mm almost overlap, while both the vanadium leaching efficiency and the growth rate of different particle sizes are different, the larger the particle size, the smaller the vanadium leaching efficiency. For the vanadium-bearing shale with the largest particle size (−3 to +2.5 mm), the vanadium leaching efficiency did not change within the activation time of 0 to 2 minutes. When the activation time increased to 4 minutes, the vanadium leaching efficiency began to increase, and the vanadium leaching efficiency shows a linear growth trend. The vanadium leaching efficiency of vanadium-bearing shale with −1 to +0.6 mm was significantly higher than that of the other three particle sizes, and the vanadium leaching increased rapidly first. When the activation time reached 6 minutes, the vanadium leaching rate was 92.57%, reaching leaching equilibrium.

3.3.2 Models establishing of vanadium leaching and activation efficiency. In order to further analyze the relationship between the yield of each particle size and the vanadium leaching efficiency, and establish the relationship equation between the yield and the vanadium leaching efficiency, as shown in Fig. 12 and Table 8. The activation yield of vanadium-bearing shale of different particle sizes with −0.6 mm has a positive linear relationship with the vanadium leaching efficiency ($R^2 = 0.98$). With the increase of the yield of the −0.6 mm particle size, the vanadium leaching efficiency also increases. The order of the growth rate of vanadium leaching efficiency

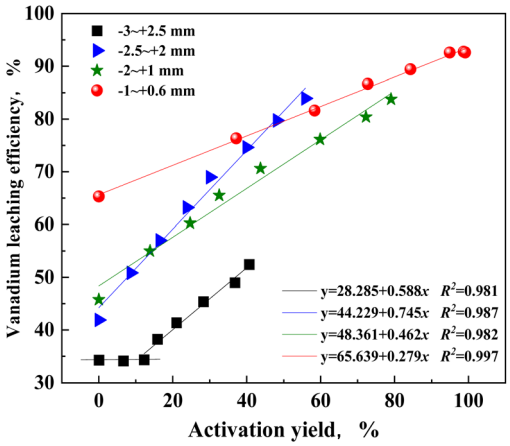

Fig. 12 Relationship between graded activation yield and vanadium leaching efficiency.

Table 8 Fitting equation and correlation coefficient of the relationship between graded activation yield and vanadium leaching efficiency

Particle size/mm	Linear equation	R^2
−3 to +2.5	$y = 28.285 + 0.588x$	0.981
−2.5 to +2	$y = 44.229 + 0.745x$	0.987
−2 to +1	$y = 48.361 + 0.462x$	0.982
−1 to +0.6	$y = 65.639 + 0.279x$	0.997

corresponding to the yield is: −3 to +2.5 mm > −2.5 to +2 mm > −2 to +1 mm > −1 to +0.6 mm.

According to the fitting equation and correlation coefficient of the relationship between the graded activation yield of vanadium-bearing shale and the vanadium leaching efficiency with the fitting accuracy reaching 0.99 in Table 8. Hence, the relationship between the activation yield and the vanadium leaching efficiency can be expressed by linear eqn (10).

$$\eta = \mu\gamma + \nu \tag{10}$$

where, η represents the vanadium leaching efficiency (%), γ represents the activation yield (%), and μ and ν are the correlation coefficients.

The eqn (1) was substituted into eqn (10) to obtain the relationship model between vanadium leaching efficiency and activation time, as shown in eqn (11).

$$\eta = \gamma_0 \exp(-kt^n)\mu + \nu \tag{11}$$

According to the activation kinetics equation of vanadium-bearing shale, the equations among the specific particle size, activation time and vanadium leaching rate of different particle sizes can be obtained.

(1) −3 to +2.5 mm:

$$\eta = 0.588 \times \gamma_0 \exp[(-0.02\exp(d/0.79) + 0.05)t^{(0.80\exp(-d/1.31)+0.39)}] + 28.285,\ 2 \le t \le 10 \tag{12}$$

(2) −2.5 to +2 mm:

$$\eta = 0.745 \times \gamma_0 \exp[(0.05\exp(d/0.78) - 0.01)t^{(1.14-0.32d)}] + 44.229,\ 0 \le t \le 10 \tag{13}$$

(3) −2 to +1 mm:

$$\eta = 0.462 \times \gamma_0 \exp[(-0.19 + 0.05d)t^{(1.14-0.68d)}] + 48.361,\ 0 \le t \le 10 \tag{14}$$

(4) −1 to +0.6 mm:

$$\eta = 0.279 \times \gamma_0 \exp(0.44t^{1.06}) + 65.639,\ 0 \le t \le 10 \tag{15}$$

3.4 The adsorption mechanism of vanadium-bearing shale in mechanochemical process

During the mechanochemical activation process, the vanadium-bearing shale will adsorb the activator simultaneously as the particle size decreases. Under the action of mechanical force, the mineral surface of vanadium-bearing shale undergoes amorphous phenomena. The atoms with unsaturated surface charges specifically adsorb F^- in the activator, reducing the surface potential of vanadium-bearing shale and increasing its hydrophilicity, promoting the adsorption and diffusion of H^+ on the mineral surface. Meanwhile, F^- is adsorbed at the central atomic positions (Si, Al) on the surface of muscovite, weakening the adjacent Si–O and Al–O bonds on the surface. During the leaching process, the weakened Si–O and Al–O bonds are prone to break during the dehydroxylation process of H^+, thereby accelerating the dissolution of muscovite during the leaching process and ultimately increasing the vanadium leaching efficiency. In order to reveal the adsorption mechanism of F^- by vanadium-bearing shale during the mechanochemical activation process, the main minerals in vanadium-bearing shale undergo mechanochemical activation using pure minerals.

3.4.1 Adsorption capacity of vanadium-bearing shale on F^-. In order to quantify the adsorption of main minerals on F^- in vanadium-bearing shale during mechanochemical processes, the adsorption content of F^- by pure minerals in the mechanochemical activation process was determined, and the results were shown in Fig. 13. The adsorption capacity of vanadium-bearing shale on F^- was 23.89 mg g^{-1}. In pure minerals, the adsorption capacity of muscovite, quartz, calcite, pyrite, feldspar and dolomite on F^- were 12.08 mg g^{-1}, 2.39 mg g^{-1}, 31.09 mg g^{-1}, 20.30 mg g^{-1}, 3.81 mg g^{-1} and 13.08 mg g^{-1}, respectively. The results showed that the main minerals in vanadium-bearing shale all adsorb F^- during the mechanochemical activation process. Among the adsorption capacity of calcite is the highest, and quartz is the lowest.

3.4.2 Surface potential of activation minerals. The zeta potential of vanadium-bearing shale before and after activation are showed in Fig. 14. After activation, the surface potential of the vanadium-bearing shale changed from positive to negative in the acidic system, which is conducive to the diffusion of H^+ to the mineral surface and promotes the dissolution of minerals. The surface potential of muscovite, quartz, feldspar and

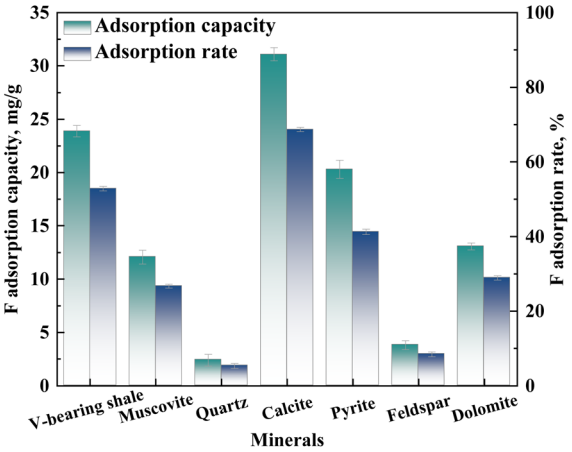

Fig. 13 F adsorption of pure minerals in vanadium-bearing shale after activation.

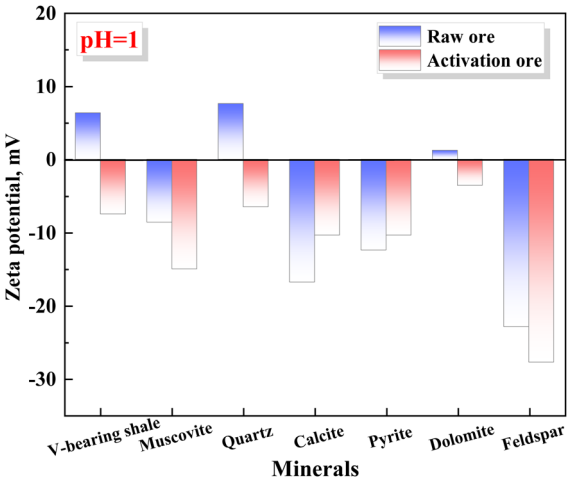

Fig. 14 Zeta potential of minerals before and after activation.

dolomite increase towards the negative potential, especially the negative charge on the surface of muscovite enhances, which is conducive to the dissolution of muscovite and thereby improves the leaching of vanadium.[32] On the contrary, the potential of calcite and pyrite decreases and the negative charge weakens, thereby weakening the competitive dissolution with muscovite.

3.4.3 Analysis of the microscopic morphology. The micromorphology of the activated pure mineral was analyzed, as shown in Fig. 15. The irregular flocculent particles of varying degrees are found on the surface of activated minerals on account of the amorphous formation of minerals in the mechanochemical activation process. In Fig. 15(a), the F^- content of muscovite surface at point A is higher than that at point B, while the sodium content at point A is lower than that at point B and the F^- content is much higher than sodium, which indicates that the adsorption of activator of muscovite in the activation process is not in the form of NaF, but in the form of ions respectively. Muscovite is one of the most representative silicate minerals, known for its nearly perfect cleavage surface, and tends to grow and dissolve along their marginal surface, which is more reactive to adsorption reactions. The (0 0 *a*) crystal surface of muscovite is a negatively charged dissociation surface, where sodium ions undergo a displacement reaction with potassium ions.[33,34] The Al–O bond and Si–O bond coated on the muscovite edge can undergo hydration reaction to form active hydroxyl group and aluminoxy group,[35–37] which combines with F to form $[SiF_6]^{2-}$ and $[AlF_5]^{2-}$. Therefore, F^- are more adsorbed on the edge surface of muscovite, which is meaningful for releasing V from the crystal lattice of muscovite. As shown in Fig. 15(b), a small amount of F^- appears in the element distribution of the surface, while F^- and Na^+ were not detected at points C and D during the spot scan. It showed that the adsorption of F^- is less during the mechanochemical activation of quartz. In Fig. 15(c), the F^- content on the dissociated surface (point E) of calcite is about 4 wt%, while the edge (point F) can reach more than 5.9 wt%, and the atomic content ratio of Ca to F is 1 : 2, indicating that the adsorption of F by calcite may result in the formation of CaF_2 adsorbed on the surface of calcite. In Fig. 15(d), the content of F^- at the adsorption points G and H on the surface of pyrite are very high, reaching more than 10%, while the content of Na^+ is zero, indicating that pyrite has a good adsorption on F^-. In Fig. 15(e), the adsorption of F^- varies greatly at I and J points of potassium feldspar. The F^- content at I point reaches 11%, while that at J point is only about 2.6%. In Fig. 15(f), the adsorption correlation of fluorine on the dolomite surface is better, but the adsorption amount is different at different locations.

3.4.4 F^- binding form in mineral surface. In order to study the adsorption state of F on the surface of various minerals, XPS was used to analyze pure minerals. The fine spectra of elements that may be combined with fluoride ions in minerals, such as Al, Si, Fe and Ca, were fitted by peak-splitting, and the results were shown in Fig. 16. The XPS fine spectrum of Si 2p and Al 2p in muscovite before and after activation were shown in Fig. 16(a) and (b), the binding energy of activation muscovite at 76.3 eV and 104.5 eV appeared new peaks, which attributed to Al $2p_{3/2}$ of Al–F and Si $2p_{3/2}$ of Si–F, indicating the F were chemically adsorbed with the active points of Si and Al on the surface of muscovite.[35,38–40] The XPS fine spectrum of Si 2p in quartz before and after activation were shown in Fig. 16(c), the binding energy of Si 2p in activated quartz widened, and the Si–F $2p_{3/2}$ peak appeared at the binding energy of 104.49 eV, indicating the activated quartz would adsorb a small amount of F.[40,41] The XPS fine spectrum of Ca 2p in calcite before and after activation were shown in Fig. 16(d). The binding energy of Ca 2p orbital in raw calcite at 347.17 eV and 350.7 eV is a double peak, which correspond to Ca $2p_{3/2}$ and Ca $2p_{1/2}$ orbits of Ca 2p, respectively. The binding energy of Ca 2p orbital in calcite after activation converted two double peaks, the new double peak at 347.98 eV and 351.5 eV correspond to Ca $2p_{3/2}$ and Ca $2p_{1/2}$ orbitals of CaF_2, respectively, which showed that a part of the surface of calcite ($CaCO_3$) were converted into CaF_2.[40,42] The XPS fine spectrum of Ca 2p in dolomite before and after activation were shown in Fig. 16(e), activated dolomite is similar to calcite, and the adsorption peaks of Ca $2p_{3/2}$ and Ca $2p_{1/2}$ orbitals of CaF_2 were generated at binding energy of 348.32 eV and 352.01 eV.[40]

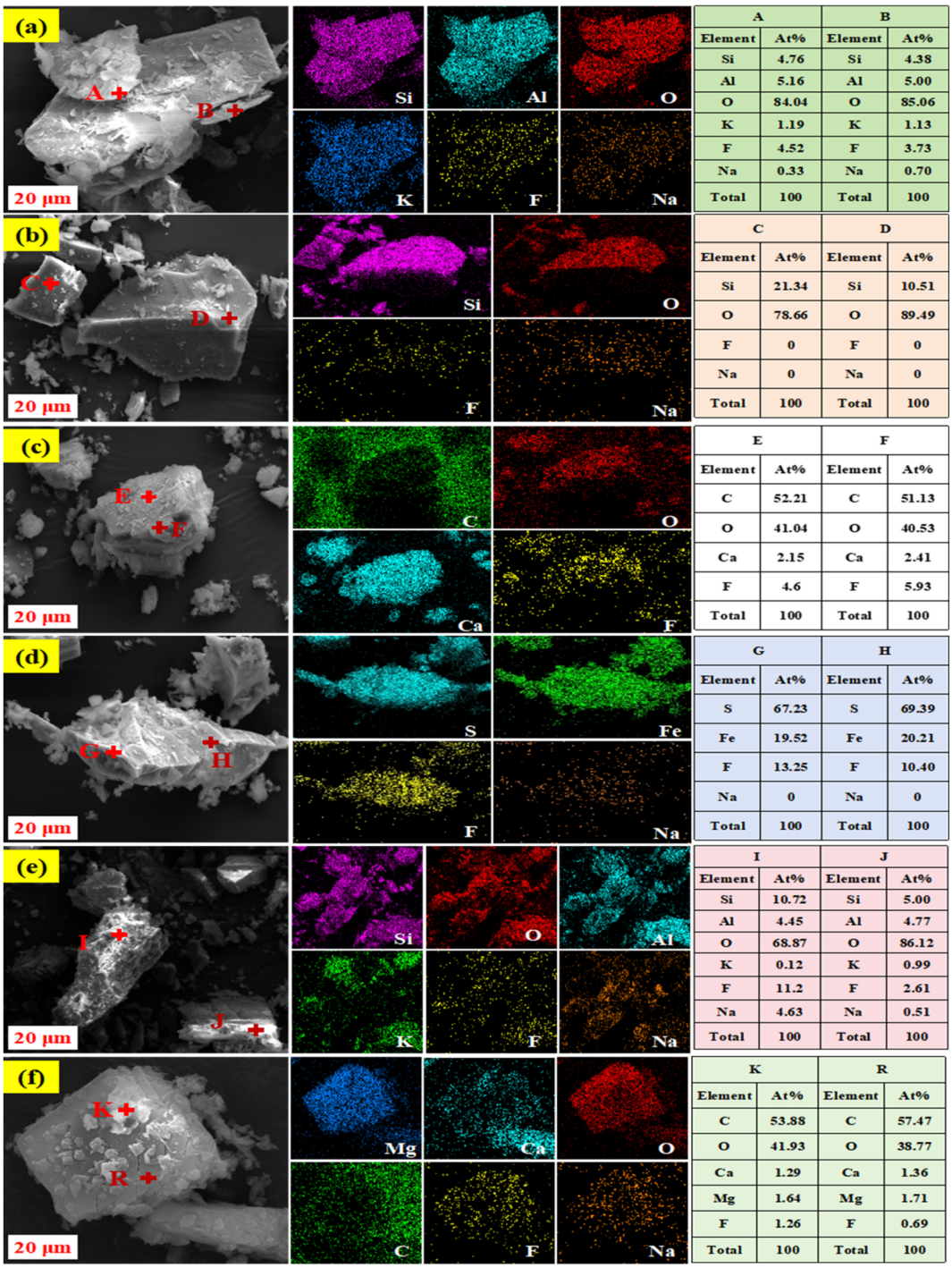

A		B	
Element	At%	Element	At%
Si	4.76	Si	4.38
Al	5.16	Al	5.00
O	84.04	O	85.06
K	1.19	K	1.13
F	4.52	F	3.73
Na	0.33	Na	0.70
Total	100	Total	100

C		D	
Element	At%	Element	At%
Si	21.34	Si	10.51
O	78.66	O	89.49
F	0	F	0
Na	0	Na	0
Total	100	Total	100

E		F	
Element	At%	Element	At%
C	52.21	C	51.13
O	41.04	O	40.53
Ca	2.15	Ca	2.41
F	4.6	F	5.93
Total	100	Total	100

G		H	
Element	At%	Element	At%
S	67.23	S	69.39
Fe	19.52	Fe	20.21
F	13.25	F	10.40
Na	0	Na	0
Total	100	Total	100

I		J	
Element	At%	Element	At%
Si	10.72	Si	5.00
Al	4.45	Al	4.77
O	68.87	O	86.12
K	0.12	K	0.99
F	11.2	F	2.61
Na	4.63	Na	0.51
Total	100	Total	100

K		R	
Element	At%	Element	At%
C	53.88	C	57.47
O	41.93	O	38.77
Ca	1.29	Ca	1.36
Mg	1.64	Mg	1.71
F	1.26	F	0.69
Total	100	Total	100

Fig. 15 The SEM images of pure minerals in vanadium-bearing shale after activation ((a): muscovite; (b): quartz; (c): calcite; (d): pyrite; (e): feldspar; (f): dolomite).

The XPS fine spectrum of Fe 2p in pyrite before and after activation were shown in Fig. 16(f), the binding energy of raw pyrite at 707.52 eV, 708.25 eV and 712.43 eV is the Fe $2p_{3/2}$ orbital, representing Fe atoms in the pyrite lattice (Fe(II)–S), surface bound Fe with S (Fe(III)–S) and oxidation products (Fe(III)–O), respectively. The binding energy at 720.33 eV and 725.98 eV correspond to spin orbits and surface oxidation products of Fe $2p_{1/2}$, respectively. The binding energy of the activated pyrite at 712.43 eV disappeared, and the Fe $2p_{3/2}$ peak of Fe(III)–F appeared at 711.17 eV, which indicated that F was adsorbed on the surface of pyrite by binding with Fe(III)–O on its surface.[40,43] After activation, the binding energies of Al 2p and Si 2p on the surface of feldspar both decreased, and the peak areas increased in Fig. 16(g) and (h). However, the characteristic peaks of Al–F and Si–F binding energies did not appeared, which indicated that the electron cloud on the surface of the surface-activated feldspar changed, and the adsorption of fluorine was not chemical adsorption.

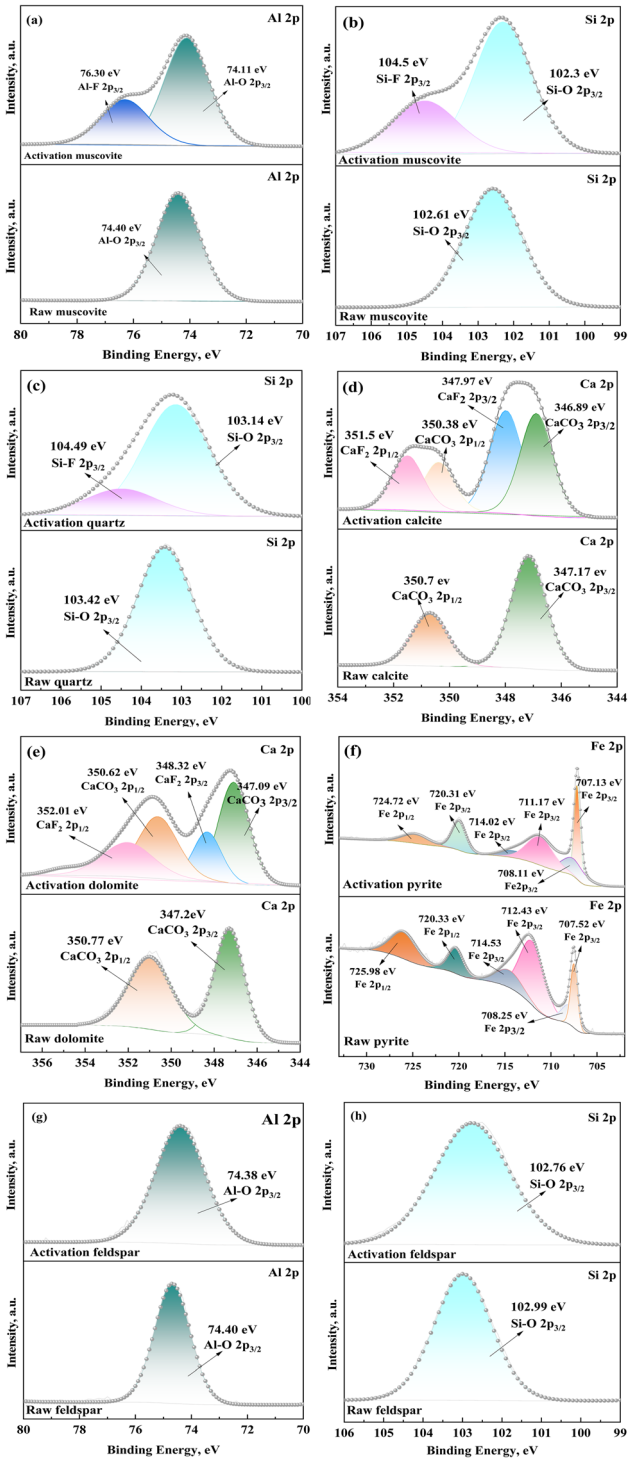

Fig. 16 XPS fine spectrum of pure minerals before and after activation ((a and b): muscovite; (c): quartz; (d): calcite; (e): dolomite; (f): pyrite; (g and h): feldspar).

4. Conclusion

This study systematically discusses process mineralogy, the optimal leaching particle size, and the kinetics of activation processes of vanadium-bearing shale. Based on the mineral characteristics of vanadium-bearing shale, a classification mechanochemical activation method was proposed. The adsorption mechanism of vanadium-bearing shale on F^- was revealed through pure minerals during the mechanochemical activation process.

(1) Vanadium-bearing shale is a complex low-grade ore, which is mainly composed of quartz, muscovite, calcite, pyrite, feldspar and apatite. Vanadium with 94.24% exists in muscovite, while the remaining 5.76% exists in oxide. Muscovite is predominantly closely associated with quartz, calcite and organic carbonaceous and tends to be enriched in fine grained, displaying fine disseminated granularity with 0.005–0.06 mm.

(2) The mineral distribution of vanadium-bearing shale of different particle sizes leads to differences in activation efficiency. The grindability order of vanadium-bearing shale is observed as follows: −3 to +2.5 mm < −2.5 to +2 mm < −2 to +1 mm < −1 to +0.6 mm. The activation process of different particle sizes were well evaluated by kinetic equations (R^2 = 0.99). The vanadium leaching efficiency has a positive linear relationship with the activation yield at the optimal leaching particle size with −0.6 mm. The vanadium leaching efficiency and activation time can be expressed by equation of $\eta = \gamma_0 \exp(-kt^n)\mu + \nu$.

(3) During the mechanochemical activation process, the mineral surface of vanadium-bearing shale undergoes amorphous phenomena, then has a good adsorption of F^- (23.89 mg g^{-1}). The order of F^- adsorption capacity is calcite, pyrite, dolomite, muscovite, feldspar, and quartz. The adsorption process of F^- alters the surface potential on the vanadium-bearing shale, especially, the negative charge on the of muscovite surface increases, while that of pyrite and calcite decreases, which is conducive to the diffusion of H^+ to the surface of muscovite and away from pyrite and calcite. F^- forms Al–F and Si–F bonds with Si and Al on the surface of muscovite, promoting the dissolution of muscovite. While F^- generates CaF_2 with the surface of calcite and FeF_3 with Fe(III)–S on the surface of pyrite, hindering and slowing down the dissolution of calcite and pyrite.

(4) The mechanochemical activation can realize the vanadium extraction by full-wet leaching with green, low-carbon and high efficiency. However, the impact of mechanochemical activation on the subsequent purification and enrichment of vanadium are further studied, especially the improvement of vanadium leaching efficiency and the accompanying leaching of impurity elements such as iron and aluminum in muscovite.

Data availability

All data included in this study are available upon request by contact with the corresponding author.

Author contributions

Xuxia Zhao: conceptualization, investigation, methodology, writing – original draft, writing – review & editing. Yimin Zhang: writing – review & editing, supervision. Nannan Xue: writing – review & editing, supervision. Pengcheng Hu: writing – review & editing, supervision.

Conflicts of interest

The authors declare that they have no known competing financial interests or personal relationships that could have appeared to influence the work reported in this paper.

Acknowledgements

This study was financially supported by National Key Research and Development Program of China (2023YFC3903900), Science and Technology Innovation Talent Program of Hubei Province (2022EJD002), National Natural Science Foundation of China (52004187 and 52174260).

References

1 W. Bo, Y. Zhang, H. Liu, *et al.*, Optimization of precursor structure by dispersants to promote nitrogen reduction process to prepare high-quality VN, *J. Alloys Compd.*, 2024, **1006**, 176285.
2 S. Dai, X. Zheng, X. Wang, *et al.*, Stone coal in China: a review, *Int. Geol. Rev.*, 2018, **60**(5–6), 736–753.
3 Y. Zhang, S. Bao, T. Liu, *et al.*, The technology of extracting vanadium from stone coal in China: History, current status and future prospects, *Hydrometallurgy*, 2011, **109**(1–2), 116–124.
4 Z. Tang, Z. Zhou, J. Jin, *et al.*, Vanadium extraction from stone coal using a novel two-stage roasting technology, *Fuel*, 2022, **321**, 124031.
5 B. Chen, S. Bao, Y. Zhang, *et al.*, A high-efficiency and sustainable leaching process of vanadium from shale in sulfuric acid systems enhanced by ultrasound, *Sep. Purif. Technol.*, 2020, **240**, 116624.
6 R. K. Asamoah, W. Skinner and J. Addai-Mensah, Leaching behaviour of mechano-chemically activated bio-oxidised refractory flotation gold concentrates, *Powder Technol.*, 2018, **331**, 258–269.
7 P. Baláž, Mechanical activation in hydrometallurgy, *Int. J. Miner. Process.*, 2003, **72**(1–4), 341–354.
8 M. Khezri, B. Rezai, A. A. Abdollahzadeh, *et al.*, Investigation into the effect of mechanical activation on the leaching of chalcopyrite in a glycine medium, *Hydrometallurgy*, 2021, **203**, 105492.
9 H. Pálková, M. Barlog, J. Madejová, *et al.*, Structural changes in smectites subjected to mechanochemical activation: The effect of the occupancy of the octahedral sites, *Appl. Clay Sci.*, 2021, **213**, 106214.
10 K. Liu, Q. Tan, L. Liu, *et al.*, Acid-Free and Selective Extraction of Lithium from Spent Lithium Iron Phosphate Batteries via a Mechanochemically Induced Isomorphic Substitution, *Environ. Sci. Technol.*, 2019, **53**(16), 9781–9788.
11 X. Geng, Y. Duan, S. Zhao, *et al.*, Mechanism study of mechanochemical bromination on fly ash mercury removal adsorbent, *Chemosphere*, 2021, **274**, 129637.
12 H. Niu, P. Kinnunen, H. Sreenivasan, *et al.*, Structural collapse in phlogopite mica-rich mine tailings induced by mechanochemical treatment and implications to alkali activation potential, *Miner. Eng.*, 2020, **151**, 106331.
13 G. Yao, T. Cui, Z. Jia, *et al.*, Effect of anhydrite on hydration properties of mechanically activated muscovite in the presence of calcium oxide, *Appl. Clay Sci.*, 2020, **196**, 105742.
14 J. Li and M. Hitch, Mechanical activation of magnesium silicates for mineral carbonation, a review, *Miner. Eng.*, 2018, **128**, 69–83.
15 A. G. Patil and S. Anandhan, Influence of planetary ball milling parameters on the mechano-chemical activation of fly ash, *Powder Technol.*, 2015, **281**, 151–158.
16 Y. Wang, X. He, Y. Su, *et al.*, Efficiency of wet-grinding on the mechano-chemical activation of granulated blast furnace slag (GBFS), *Constr. Build. Mater.*, 2019, **199**, 185–193.
17 T. C. Alex, R. Kumar, S. K. Roy, *et al.*, Mechanically induced reactivity of gibbsite: Part 1. Planetary milling, *Powder Technol.*, 2014, **264**, 105–113.
18 W. Zhou, Y. Han, Y. Sun, *et al.*, Multi-scale impact crushing characteristics of polymetallic sulphide ores, *Trans. Nonferrous Met. Soc. China*, 2019, **29**(9), 1929–1938.
19 Y. P. Singh, H. Tanvar, G. Kumar, *et al.*, Investigation of planetary ball milling of sericite for potash recovery, *Powder Technol.*, 2019, **351**, 115–121.
20 J. Yu, Y. Qin, P. Gao, *et al.*, An innovative approach for determining the grinding media system of ball mill based on grinding kinetics and linear superposition principle, *Powder Technol.*, 2021, **378**, 172–181.
21 L. Wang, H. Wang, J. Zhu, *et al.*, Experimental study on particle size distribution of impact crushed coal containing gas, *Fuel*, 2022, **325**, 124745.
22 N. A. Miele, A. Borriello, M. Fidaleo, *et al.*, Modeling grinding kinetics of fat based anhydrous pastes, *J. Food Eng.*, 2020, **268**, 109732.
23 R. Zhao, Y. Han, M. He, *et al.*, Grinding kinetics of quartz and chlorite in wet ball milling, *Powder Technol.*, 2017, **305**, 418–425.
24 P. Li, Z. Cao, R. Zhao, *et al.*, The kinetics and efficiency of batch ball grinding with cemented tungsten carbide balls, *Adv. Powder Technol.*, 2020, **31**(6), 2412–2420.
25 V. K. Gupta, Effect of particulate environment on the grinding kinetics of mixtures of minerals in ball mills, *Powder Technol.*, 2020, **375**, 549–558.
26 X. Zhao, Y. Zhang, N. Xue, *et al.*, Effect of mechano-chemical activation with NaF on improved acid leaching of vanadium-bearing shale, *Hydrometallurgy*, 2023, **221**, 106126.
27 Z. H. Wang, F. J. Yu, S. Cai, *et al.*, Effect of Grinding Aids on the Fracture Energy of Mica, *Adv. Mater. Res.*, 2011, **402**, 503–509.
28 J. Duroudier, Appendix 1-Mohs Scale, *Divided Solids Transport*, 2016, pp. 153–155.
29 H. Wang, C. Ju, M. Zhou, *et al.*, Grinding kinetics of lead–zinc tailing powders and its optimal particle size as a pozzolanic admixture in cement mortar, *Adv. Powder Technol.*, 2022, **33**(9), 103730.
30 Y. Qin, Y. Han, P. Gao, *et al.*, Characterization of chalcopyrite ore under high voltage pulse discharge: Particle size distribution, fractal dimension, specific energy

consumption, grinding kinetics, *Miner. Eng.*, 2022, **184**, 107631.
31 H. Choi, J. Lee, H. Hong, *et al.*, New evaluation method for the kinetic analysis of the grinding rate constant via the uniformity of particle size distribution during a grinding process, *Powder Technol.*, 2013, **247**, 44–46.
32 Q. Xu, Y. Sun, L. Yang, *et al.*, Leaching mechanism of ion-adsorption rare earth by mono valence cation electrolytes and the corresponding environmental impact, *J. Cleaner Prod.*, 2019, **211**, 566–573.
33 W. de Poel, S. L. Vaessen, J. Drnec, *et al.*, Metal ion-exchange on the muscovite mica surface, *Surf. Sci.*, 2017, **665**, 56–61.
34 P. Frank, G. Hlawacek, O. Lengyel, *et al.*, Influence of surface temperature and surface modifications on the initial layer growth of para-hexaphenyl on mica (001), *Surf. Sci.*, 2007, **601**(10), 2152–2160.
35 D. Bhowmik and P. Karmakar, Tailoring and investigation of surface chemical nature of virgin and ion beam modified muscovite mica, *Surf. Interface Anal.*, 2019, **51**(6), 667–673.
36 C. Elmi, M. F. Brigatti, S. Guggenheim, *et al.*, Sodian muscovite-2M1: Crystal chemistry and surface features, *Can. Mineral.*, 2013, **51**(1), 5–14.
37 G. Yao, T. Cui, Y. Su, *et al.*, Hydration properties of mechanically activated muscovite in the presence of calcium oxide, *Clays Clay Miner.*, 2020, **68**(6), 580–587.
38 C. Elmi, S. Guggenheim and R. Gieré, Surface crystal chemistry of phyllosilicates using X-ray photoelectron spectroscopy; a review, *Clays Clay Miner.*, 2016, **64**(5), 537–551.
39 S. A. Saslow Gomez and F. M. Geiger, Precipitates of Al(III), Sc(III), and La(III) at the Muscovite–Water Interface, *J. Phys. Chem. A*, 2014, **118**(46), 10974–10981.
40 NIST XPS Database, **https://srdata.nist.gov/xps/selEnergyType.aspx**, 2025.
41 Z. Ding, J. Li, J. Yuan, *et al.*, Insights into the influence of calcium ions on the adsorption behavior of sodium oleate and its response to flotation of quartz: FT-IR, XPS and AMF studies, *Miner. Eng.*, 2023, **204**, 108437.
42 X. Yang, Y. Li, J. Chen, *et al.*, Enhanced flotation separation of fluorite and F^--activated calcite by sodium gluconate and sodium silicate, *Miner. Eng.*, 2025, **229**, 109375.
43 P. Hu, Y. Zhang, T. Liu, *et al.*, Source separation of vanadium over iron from roasted vanadium-bearing shale during acid leaching via ferric fluoride surface coating, *J. Cleaner Prod.*, 2018, **181**, 399–407.